ACS APPLIED MATERIALS & INTERFACES

Research Article

www.acsami.org

Loading $Cd_{0.5}Zn_{0.5}S$ Quantum Dots onto Onion-Like Carbon Nanoparticles to Boost Photocatalytic Hydrogen Generation

Xiaolong Zhou,[†] Xina Wang,*[,†] Xi Feng,[‡] Kun Zhang,[§] Xiaoniu Peng,[†] Hanbin Wang,[†] Chunlei Liu,[†] Yibo Han,[§] Hao Wang,[†] and Quan Li*[,§]

[†]Hubei Collaborative Innovation Center for Advanced Organic Chemical Materials, Hubei Key Laboratory of Ferro & Piezoelectric Materials and Devices, Faculty of Physics and Electronic Science, Hubei University, Wuhan 430062, China

[‡]Department of Physics, The Chinese University of Hong Kong, Hong Kong, China

[§]Wuhan National High Magnetic Field Center and School of Physics, Huazhong University of Science and Technology, Wuhan 430072, China

Supporting Information

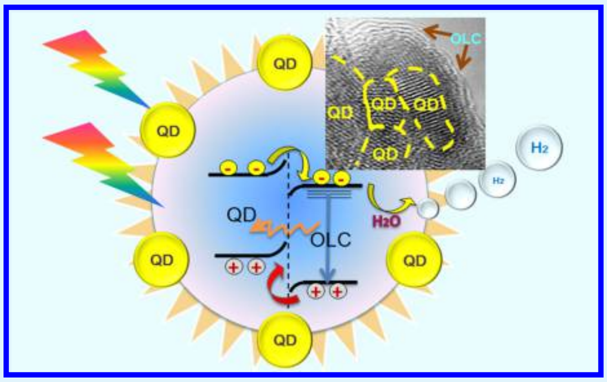

ABSTRACT: Carbon dots (C dots, size < 10 nm) have been conventionally decorated onto semiconductor matrixes for photocatalytic H_2 evolution, but the efficiency is largely limited by the low loading ratio of the C dots on the photocatalyst. Here, we propose an inverse structure of $Cd_{0.5}Zn_{0.5}S$ quantum dots (QDs) loaded onto the onionlike carbon (OLC) matrix for noble metal-free photocatalytic H_2 evolution. $Cd_{0.5}Zn_{0.5}S$ QDs (6.9 nm) were uniformly distributed on an OLC (30 nm) matrix with both upconverted and downconverted photoluminescence property. Such an inverse structure allows the full optimization of the QD/OLC interfaces for effective energy transfer and charge separation, both of which contribute to efficient H_2 generation. An optimized H_2 generation rate of 2018 μmol/h/g (under the irradiation of visible light) and 58.6 μmol/h/g (under the irradiation of 550−900 nm light) was achieved in the $Cd_{0.5}Zn_{0.5}S$/OLC composite samples. The present work shows that using the OLC matrix in such a reverse construction is a promising strategy for noble metal-free solar hydrogen production.

KEYWORDS: *onionlike carbon, photocatalyst, H_2 evolution, $Cd_{0.5}Zn_{0.5}S$, nanoparticles, quantum dots*

1. INTRODUCTION

Among the various photocatalysts for hydrogen generation, $Cd_{0.5}Zn_{0.5}S$ has attracted extensive attention because of its tunable band gap (from 2.3 to 3.6 eV), high photochemical stability, and low cost.[1−3] An optimal Zn content of ∼0.5 was determined for the optimum photocatalytic property.[4,5] Unfortunately, the hydrogen production by employing $Cd_{0.5}Zn_{0.5}S$ alone is not satisfactory, and cocatalysts such as Pt, CoPt, Au, and RuS_2 are usually required for lowering the energy barrier of the water reduction half reaction,[6−9] thus enhancing the hydrogen production. With Au as the cocatalyst, the highest photocatalytic H_2 generation achieved is ∼6.3 mmol/h/g.[8] However, the noble metal components in the cocatalyst make it expensive, limiting its potential large-scale applications in solar fuel generation.

Much effort has been devoted to develop a noble metal-free cocatalyst, and carbon-based materials are proposed as promising candidates. Both reduced graphene oxide (rGO) and carbon nanotubes are found to function as effective reservoirs and transporters of the photoelectrons generated in the photocatalysts such as $Cd_{0.5}Zn_{0.5}S$ and TiO_2, which inhibits charge recombination and enhances the photocatalytic property.[10−12] Carbon dots (CDs) including nanodiamond (ND), graphene quantum dot (GQD), carbon quantum dot (CQD), and onionlike carbon (OLC) nanoparticles serve as another family of cocatalyst candidates for solar hydrogen production.[13−18] Both down and upconverted photoluminescence (PL) have been demonstrated in CDs.[19−23] The downconverted PL (DCPL) property of CDs makes it possible for photocatalytic applications if the photoexcited charge carrier can be effectively separated before their recombination, whereas the upconverted PL (UCPL) suggests the possibility of using CDs to absorb longer wavelength photons and excite a photocatalyst with the band gap energy of a shorter wavelength. In fact, increased light absorption in both the visible and near infrared (NIR) region has been found when CDs are coupled with photocatalysts such as TiO_2,[15,24,25] $ZnIn_2S_4$,[26] WO_3,[27] $Ag_3PW_{12}O_{40}$,[28] C_3N_4,[13,29] and Cu_2O.[30−32] In all reported works, small-sized CDs (usually ≤10 nm) are loaded onto a relatively large photocatalyst matrix. The low loading capacity (CD/photocatalyst volume ratio <1:1000) greatly limits

Received: April 24, 2017
Accepted: June 16, 2017
Published: June 16, 2017

DOI: 10.1021/acsami.7b05592
ACS Appl. Mater. Interfaces 2017, 9, 22560−22567

any possible enhancements in H_2 generation (maximum 1.6 mmol/h/g achieved without additional noble metal cocatalysts). Compared with ND and CQD, the size of the OLC can be extended to several tens of nanometers, for example, ~40 nm,[21,33] which makes it possible for the OLC to serve as a matrix to load the photocatalytic QDs and allows the manipulation of the OLC to QD ratio (and therein, the interfaces between the two of them). Unfortunately, such a configuration has been rarely investigated until now.

In the present work, we show that the OLC nanoparticles with an average size of 30 nm have both DCPL and UCPL properties. They serve as effective matrix materials for loading $Cd_{0.5}Zn_{0.5}S$ QDs, allowing the ratios between the OLC and the $Cd_{0.5}Zn_{0.5}S$ QDs to be systematically varied. This leads to the optimization of the OLC to the $Cd_{0.5}Zn_{0.5}S$ QD ratio, when effective charge separation/transfer at the $Cd_{0.5}Zn_{0.5}S$/OLC interface and energy transfer from the OLC to the QDs are achieved. Photocatalytic H_2 generation rates of 2018 μmol/h/g upon the irradiation of visible light and 58.6 μmol/h/g upon the irradiation of long-wavelength light have been demonstrated. The charge separation and energy transfer mechanism between the OLC and the QDs are discussed in detail based on the studies of band alignment, loading density-dependent hydrogen evolution property, and PL lifetime.

2. EXPERIMENTAL SECTION

2.1. Chemicals and Materials. All chemicals used in this study were of reagent grade and used without further purification. Cadmium chloride ($CdCl_2\cdot 2.5H_2O$, ≥99%, analytical reagent, Sinopharm), zinc chloride ($ZnCl_2$, ≥98%, analytical reagent, Sinopharm), sodium sulfide ($Na_2S\cdot 9H_2O$, ≥98%, analytical reagent, Maclin), polyvinyl alcohol ($[C_2H_4O]_n$, ≥99%, Sinopharm), sodium hydroxide (NaOH, ≥96%, analytical reagent, Sinopharm), hydrochloric acid (HCl, 36.5−38%, analytical reagent, Sinopharm), and sodium sulfite anhydrous (Na_2SO_3, ≥98%, analytical reagent, Sinopharm) were used as received. Solutions were prepared using high purity water (Milli-Q purification system, resistivity > 18 MΩ·cm). Fluorine-doped tin oxide (FTO) coated glass (<14 Ω, 20 mm × 20 mm) and platinum plate were purchased for the experiment.

2.2. Synthesis of Catalysts. To prepare the OLC, 40 mL aqueous solution containing 1 g sodium hydroxide and 1 g polyvinyl alcohol (PVA, M_w: 1750) was transferred to a Teflon autoclave and heated at 250 °C for 10 h. After it was naturally cooled down to room temperature, large particles were filtered away from the obtained solution and a transparent brown solution was left. Then, dilute hydrochloric acid was added in the brown solution to remove the byproducts and centrifuged at 6000 rpm for 5 min to obtain the OLC nanoparticles, after which the nanoparticles were dissolved in 10 mL ethanol for further synthesis of the nanocomposites.

To synthesize the $Cd_{0.5}Zn_{0.5}S$/OLC nanocomposites that are named $Cd_{0.5}Zn_{0.5}S/xC$ samples (x = 1, 2, 3, 4, 5), x mL OLC nanoparticles solution was added to a 20 mL ethylene glycol solution containing 272.6 mg $ZnCl_2$ and 456.7 mg $CdCl_2\cdot 2.5H_2O$. The mixed solution was stirred continuously under the protection of nitrogen and heated to 170 °C, and then, 20 mL ethylene glycol solution dissolving 960.7 mg $Na_2S\cdot 9H_2O$ was quickly added. The solution was heated to 180 °C and held for 1 h for the growth of $Cd_{0.5}Zn_{0.5}S$ QDs on the OLC. The $Cd_{0.5}Zn_{0.5}S/xC$ composites were collected by centrifugation, washed using ethanol and deionized water 3 times, and dried in a vacuum oven at 70 °C for 12 h. For pure $Cd_{0.5}Zn_{0.5}S$ QDs, the method is similar to that of the composites except for the addition of the OLC.

2.3. Material Characterization. The microstructure and compositional distribution of the samples were studied by a transmission electron microscope (TEM, FEI Tecnai 20) equipped with scanning transmission electron microscopy (STEM), energy-dispersive X-ray spectroscopy (EDS), and electron energy loss spectroscopy (EELS). The crystallinity was characterized by X-ray diffraction (XRD, Bruker D8). The element composition, chemical states, and valence states were studied by (valence band, VB) X-ray photoelectron spectroscopy (XPS) measurements (ESCALAB 250Xi) with Al Kα radiation. The detailed functional groups of the samples were studied by a Fourier transform infrared (FTIR) spectrometer (Thermo-Nicolet Nexus 670). The absorption property was studied by an UV−vis spectrophotometer equipped with an integrating sphere device (UV-3600, Shimadzu). Fluorescence measurements were performed by a 7000 FL spectrophotometer (Hitachi, F7000). The PL lifetime measurements were carried out by open- and closed-aperture Z-scan techniques, in which a Ti:sapphire laser (Coherent, Mira 900) with the pulse duration of 130 fs and the repetition rate of 76 MHz was used as the laser source. The Raman spectra were recorded with a spectral resolution of 0.5 cm^{-1} using a Raman system (JY, HR-800) at a power of 0.1 mW, and the 532 nm line of a Nd^{3+}:YAG laser was used for excitation.

2.4. Photoelectrochemical and Electrochemical Characterizations. Mott−Schottky measurements were conducted in 0.5 M Na_2SO_4 electrolyte (pH = 6.8) in an electrochemical work station (CHI 760E, CH Instruments) with a typical three-electrode configuration. A Pt foil and saturated Ag/AgCl were used as the counter and reference electrodes. The working electrode was fabricated by spreading the paste of 2 mg sample and 1 mg polyethylene glycol (M = 20 000) in 1 mL ethanol onto 1 cm^2 area of the FTO substrate, then annealed at 450 °C for 30 min. The potentials were converted to those versus reversible hydrogen electrode (RHE) via the equation E (vs RHE) = E (vs Ag/AgCl) + $E_{Ag/AgCl}$ (ref) + 0.0591 V × pH, where [$E_{Ag/AgCl}$ (ref) = 0.1976 V vs normal hydrogen electrode at 25 °C]. Transient photocurrent on−off cycles were carried out in the similar three-electrode system except for the electrolyte that was composed of 0.35 M Na_2SO_3 and 0.25 M Na_2S aqueous solution. In the transient photocurrent measurements, the working electrode was applied at a bias of 0.5 V_{RHE}, AM 1.5G light (CEL-HXF300) with an AM 1.5G filter was used as the illumination source, and the incident power was maintained at 100 mW/cm^2. Electrochemical impedance spectra (EIS) were measured at a bias of 0.5 V_{RHE} in the dark with an amplitude of 5 mV in a frequency range from 0.1 Hz to 100 kHz.

The Mott−Schottky relationship is derived by solving Poisson's equation for a depleted semiconductor space-charge layer with the imposition of many assumptions and simplifications, which can be expressed as $C^{-2} = (2/\varepsilon\varepsilon_0 eNA^2)\cdot(E - E_{FB} - kT/e)$, where C is the space-charge capacitance, ε is the dielectric constant, ε_0 is the permittivity of free space, e is the charge on the electron, N is the carrier density, A is the sample area, E is the impressed voltage, E_{FB} is the flat band potential, T is the temperature, and k is Boltzmann's constant.

2.5. Photocatalytic H_2 Evolution. The evaluation system of photocatalytic H_2 generation is shown in Figure S1. First, 0.1 g sample dispersed in 100 mL aqueous solution of 0.35 M Na_2SO_3 and 0.25 M Na_2S was kept under continuous mechanical stirring and was degassed by N_2 for 30 min to remove the remnant air (Figure S1a), and the flask reactor had a volume of 150 mL. Then, the hydrogen evolution experiments were performed under the visible light irradiation of a 300 W Xe lamp (CEAULIGHT) with a long-pass filter (420 nm, Newport) and incident power of 300 mW/cm^2, in which the distance between the radiation source and the reactor was kept 30 cm (Figure S1b). For contrast, the hydrogen evolution under 420−550 and 550−900 nm region light was carried out via different edge filters while keeping other conditions unchanged; then, an incident power of ~160 and ~80 mW/cm^2 was realized for 420−550 and 550−900 nm range light, respectively. The hydrogen generation was analyzed using a gas chromatograph (GC-2018, Shimadzu, Japan, TCD, Figure S1c), which adopts N_2 as a carrier. The apparent quantum efficiency (AQE) was evaluated at 420 nm using the following equation[34]

$$\mathrm{AQE}\ (\%) = \frac{\text{number of reacted electrons}}{\text{number of incident photons}} \times 100\%$$

$$= \frac{2 \times \text{number of evolved}H_2\text{ molecules}}{\text{number of incident photons}} \times 100\%$$

3. RESULTS AND DISCUSSIONS

3.1. Morphology, Structure, and Surface Chemical States. Before loading $Cd_{0.5}Zn_{0.5}S$ QDs onto the OLC nanoparticles, the morphologies of each of them were studied by TEM, as shown in Figure 1. The OLC nanoparticles with an average diameter of ~30 nm are shown in Figure 1a. The high-resolution TEM images (Figure 1b) show that the "onions" are defective and disordered, consisting of concentric multiple shells. The separation between the shells is ~0.41 nm, slightly larger than that of the bulk graphite. Figure 1c,d shows the TEM images of pure $Cd_{0.5}Zn_{0.5}S$ QDs. These QDs have an average diameter of 6.7 ± 0.9 nm with a very narrow distribution (5−9 nm) as presented in Figure S2. The observed lattice spacings of 0.32 and 0.35 nm are consistent with the respective interlayer distance of (002) and (100) planes of the hexagonal $Cd_{0.5}Zn_{0.5}S$ (PDF no. 89-2943, Figure S3). This agrees with the selected area electron diffraction (SAED) patterns shown in the inset of Figure 1c. The EDS spectrum indicates a molar ratio of 1:1:2 for Cd/Zn/S. It is noticeable that the surface of the QD is sharp without any amorphous layers.

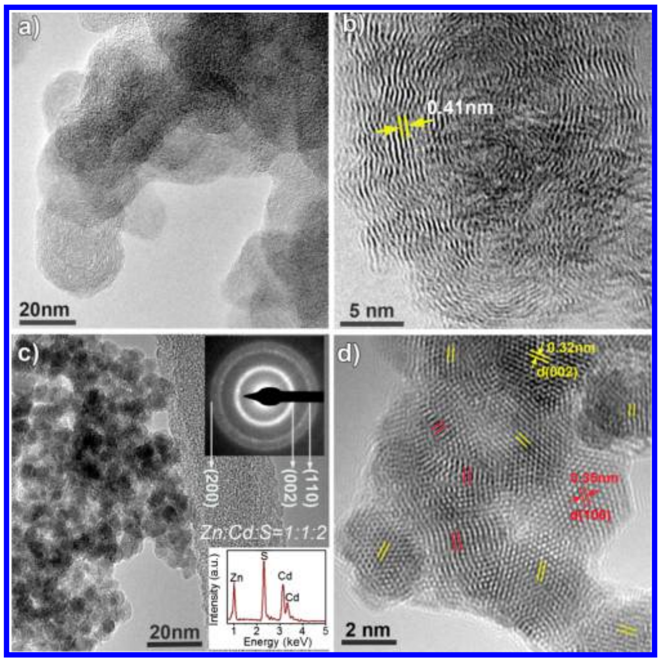

Figure 1. Microstructure and elemental composition of pure OLC and $Cd_{0.5}Zn_{0.5}S$ QDs. (a) Low-magnification and (b) high-resolution TEM images of the OLC. (c) Low-magnification and (d) high-resolution TEM images of pure $Cd_{0.5}Zn_{0.5}S$ QDs (inset: SAED pattern and EDS spectrum), and the yellow and red marks correspond to (100) and (002) planes, respectively.

$Cd_{0.5}Zn_{0.5}S$ QDs are loaded onto the OLCs to form the $Cd_{0.5}Zn_{0.5}S$/OLC composition with different $Cd_{0.5}Zn_{0.5}S$/OLC ratios (see Methods). These samples have similar morphologies and structures, and Figure 2 shows a representative example of sample $Cd_{0.5}Zn_{0.5}S$/3C. Figure 2a−c show the TEM images of discrete $Cd_{0.5}Zn_{0.5}S$ QDs uniformly distributed on the OLC particles at different magnifications. The OLCs maintain the onionlike skeleton, whereas the $Cd_{0.5}Zn_{0.5}S$ QDs remain hexagonal, which is consistent with the XRD results (Figure S3). From Figure 2c, though most of the OLC surfaces have been covered by QDs, a few graphitelike layers can be distinguished at the outer boundary of the QDs. Unlike their freestanding counterparts, the $Cd_{0.5}Zn_{0.5}S$ QDs are no longer in close contact with each other after being loaded onto the OLC. That is to say, the interface between the individual QDs are now replaced by interfaces between the QDs and the OLCs. Little diffraction signal is obtained for the OLC in the XRD, suggesting its poor crystalline quality. The uniform distribution of the $Cd_{0.5}Zn_{0.5}S$ QDs and the OLC is suggested by the EELS mappings of C, Cd, Zn, and S (Figure 2d−h).

The OLC is known for its rich surface functional groups. XPS taken from the pure OLC sample is shown in Figure 3a. Fitting of the XPS data suggests the presence of a few peaks at 284.6, 285.4, 286.2, 286.8, 288.7, and 289.3 eV, corresponding to the bondings of sp^2 C=C, sp^3 C−C, C−H, C−O, C=O, and COOH, respectively, indicating the presence of various oxygenated chemical functional groups.[29,32,33] The coexistence of sp^2 and sp^3 is consistent with the onionlike structure as shown in the TEM pictures, in which the onion shells agree well with the graphitelike structure of sp^2 C, whereas the numerous defects indicate the formation of sp^3 C. The presence of C=O, C−OH, and C−H functional groups in the OLC are further confirmed by the FTIR

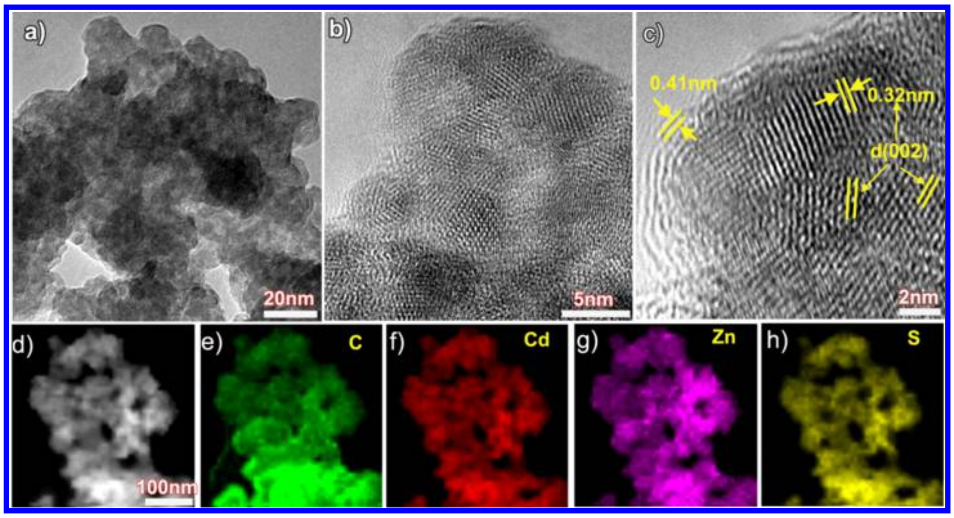

Figure 2. Microstructure and elemental composition of $Cd_{0.5}Zn_{0.5}S$/OLC composites. (a−c) Different magnified TEM image, (d) high-angle annular dark field (HAADF)-STEM image, and (e−h) the corresponding EELS mappings of $Cd_{0.5}Zn_{0.5}S$/OLC composites.

DOI: 10.1021/acsami.7b05592
ACS Appl. Mater. Interfaces 2017, 9, 22560−22567

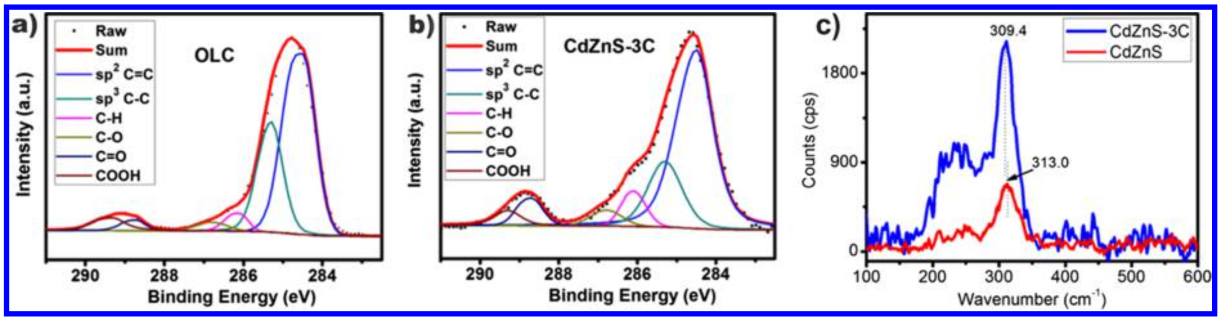

Figure 3. Valence state of C evolved with the composition with $Cd_{0.5}Zn_{0.5}S$ QDs and the Raman shift of the QDs before and after the loading onto OLC. (a) XPS fine scans of C 2p from pure OLC and (b) $Cd_{0.5}Zn_{0.5}S$/OLC composites. (c) Raman spectra of pure $Cd_{0.5}Zn_{0.5}S$ and the $Cd_{0.5}Zn_{0.5}S$/3C composite.

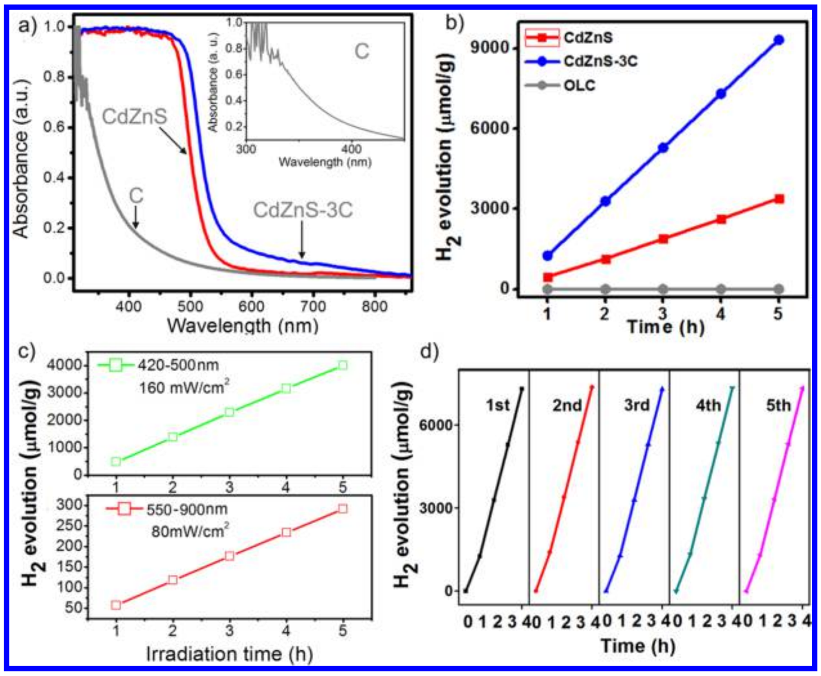

Figure 4. Photocatalytic property of the samples. (a) UV−vis absorption spectra of the OLC, $Cd_{0.5}Zn_{0.5}S$, and $Cd_{0.5}Zn_{0.5}S$/OLC nanocomposites. (b,c) Time-dependent H_2 evolution rate under the irradiation of visible and different range of light. (d) Cycling tests of $Cd_{0.5}Zn_{0.5}S$/OLC nanocomposites under the irradiation of visible light.

spectrum (Figure S4a). Obvious vibrations of surface hydroxyl functional groups (~3436 cm^{-1}), oxygenated functional groups including C═O (1714, 1625 cm^{-1}), C−O−C (1199 and 1100 cm^{-1}), C−O−H bonds (1163 and 1263 cm^{-1}), and CH_x groups such as sp^3-CH_3, sp^3-CH_2, and sp^3-CH have been detected. After loading $Cd_{0.5}Zn_{0.5}S$ QDs onto the OLC, strong Cd−S and Zn−S bond vibrations can be detected in the low-frequency region of FTIR (Figure S4b), which reduce the relative absorption of the OLC. From the fine XPS of the $Cd_{0.5}Zn_{0.5}S$/3C composite (Figure 3b), besides the vibration peaks of the functional groups, it is worth mentioning that the sp^3 C−C content (285.4 eV) slightly decreases compared with the sp^2 C−C bonds (284.6 eV) after the loading of $Cd_{0.5}Zn_{0.5}S$ QDs, suggesting the QDs tend to occupy the C sites with sp^3 hybridization. The interaction of the OLC with $Cd_{0.5}Zn_{0.5}S$ QDs can also be reflected by the Raman shift as presented in Figure 3c. The LO phonon mode of pure $Cd_{0.5}Zn_{0.5}S$ QDs at 313.0 cm^{-1} will shift to a lower energy of 309.4 cm^{-1} after the QDs are loaded onto the OLC,[35] indicating the existence of the strain induced by the $Cd_{0.5}Zn_{0.5}S$/OLC interface. It is noticeable that the typical Raman signal of carbon (D and G modes) at a higher energy side for both the OLC and the $Cd_{0.5}Zn_{0.5}S$/OLC composite cannot be distinguished because of the strong fluorescence from the OLC. The fluorescence can also be reflected at the lower energy region (180−280 cm^{-1}) in Figure 3c.

3.2. Absorption and Photocatalytic Property.

The coupling of $Cd_{0.5}Zn_{0.5}S$ and the OLC in the composite leads to changes in the absorption property (Figure 4a). Pure OLC has an obvious peak appearing at ~330 nm (Figure 4a and inset) because of the n−π* transition of C═O bonds.[36] Its absorption quickly decays at a longer wavelength with a cut-off value of ~500 nm. Pure $Cd_{0.5}Zn_{0.5}S$ QDs have a typical absorption edge at ~506 nm, corresponding to an optical band gap of 2.45 eV, as estimated from the Tauc plot as shown in Figure S5. After forming $Cd_{0.5}Zn_{0.5}S$/OLC nanocomposites, the absorption edge gradually shifts to a longer wavelength of 530 nm, and an obvious absorption tail extending to a longer wavelength region (510−850 nm) can be found, suggesting the enhanced absorption of the composite in the visible and the NIR range.

The photocatalytic hydrogen evolution of such a sample is investigated upon light irradiation at three different wavelength ranges (i.e., ≥420, 420−550, and 550−900 nm). Figure 4b shows

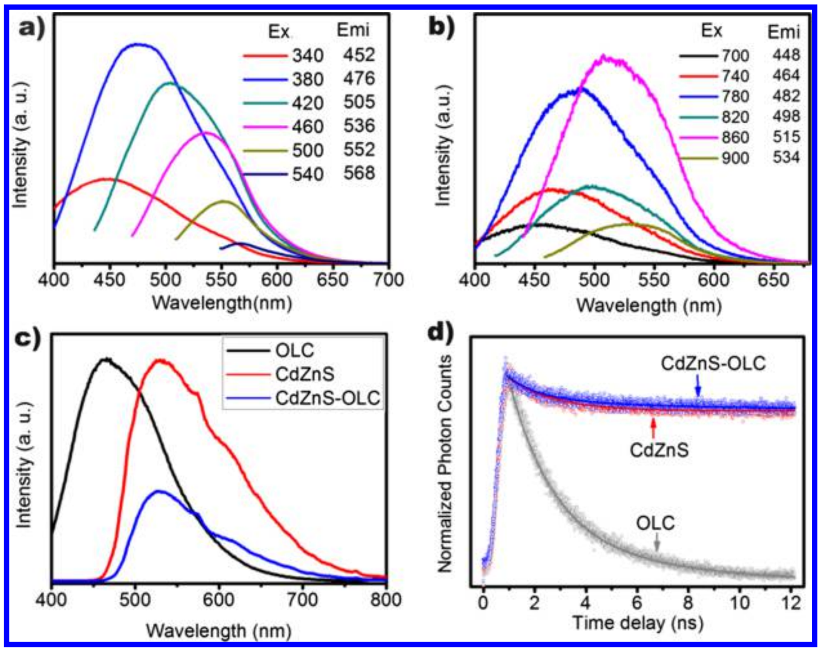

Figure 5. PL characterization before and after the composition of the OLC and $Cd_{0.5}Zn_{0.5}S$ QDs. (a,b) Fluorescence of pure OLCs excited by various wavelength light. (c,d) PL spectra and lifetime measurement of pure OLC, $Cd_{0.5}Zn_{0.5}S$ QDs, and $Cd_{0.5}Zn_{0.5}S$/OLC composites under excitation light of 380 nm.

the hydrogen generation of $Cd_{0.5}Zn_{0.5}S$ QDs and $Cd_{0.5}Zn_{0.5}S$/OLC nanocomposites under light irradiation of wavelength ≥420 nm powered at 300 mW/cm^2. The amount of hydrogen generated from both $Cd_{0.5}Zn_{0.5}S$/OLC composites and pure QDs linearly increases with the illumination time, and performance enhancement is found in the composite sample. A hydrogen evolution reaction (HER) rate of 2018 μmol/h/g is achieved for the $Cd_{0.5}Zn_{0.5}S$/3C nanocomposites, which is about threefold that of pure $Cd_{0.5}Zn_{0.5}S$ (732 μmol/h/g). On the other hand, the OLC alone does not produce an appreciable amount of hydrogen under the same conditions, which might be caused by the fast recombination of the photoexcited electrons and holes via the defect levels, very similar to the behavior of pure nanodiamonds.[32] It is important to note that the $Cd_{0.5}Zn_{0.5}S$/OLC sample exhibits an obvious photoresponse in the longer wavelength range (Figure 4c). A HER rate of 58.6 μmol/h/g is observed when irradiated under 550−900 nm light for 5 h. Although such a rate is much lower than that obtained under the irradiation of the 420−550 nm wavelength light (881.4 μmol/h/g), the appreciable response to long-wavelength light suggests its possible correlation with the improved absorption of the composition in the NIR region. As a comparison, the HER generation is negligible for pure $Cd_{0.5}Zn_{0.5}S$ under the 550−900 nm light irradiation. Furthermore, the recycling HER test for the nanocomposites in Figure 3d shows little deterioration in the HER behavior after five cycles, suggesting a high photostability for potential applications. The apparent quantum yield at 420 nm of pure $Cd_{0.5}Zn_{0.5}S$ QDs is ∼17.3%, which is increased to ∼43.2% after the QDs are loaded onto the OLC ($Cd_{0.5}Zn_{0.5}S$/3C). Such an efficiency is superior than that of Pt/$Cd_{1-x}Zn_xS$/ZnO/$Zn(OH)_2$ (12.4%), CdSe/CdS−Au (25.4%), Pt/CdS (31.5%), and MoS_2/CdS (41.4%) heterostructures.[37−40]

3.3. PL Property. Generally speaking, the photon-induced charge-carrier generation, separation, transfer, and recombination processes are critical in determining the photocatalytic H_2 generation. In this regard, we first studied the PL of the OLC, $Cd_{0.5}Zn_{0.5}S$ QDs, and the $Cd_{0.5}Zn_{0.5}S$/3C composite samples. Pure OLC nanoparticles show excitation wavelength-dependent luminescence (Figure 5a,b). Little emission is detectable for excitation wavelength (λ_{ex}) < 300 nm. A red shift in the emission wavelength (λ_{em}) of the OLC from 452 to 568 nm is observed as the λ_{ex} increases from 340 to 540 nm. The emission peaks are wide and a maximum intensity is reached at $\lambda_{ex} \approx 380$ nm. On the other hand, the OLC nanoparticles show typical UCPL property. Short wavelength emissions ranging from 448 to 534 nm are collected when the excitation wavelength varies from 700 to 900 nm. The emission wavelength partially overlaps with the absorption range of $Cd_{0.5}Zn_{0.5}S$ QDs, making it possible for the OLC emission to serve as the secondary excitation source for QDs, leading to additional charge-carrier generation. Given that the wavelength-tunable emission of most CDs can be contributed to the intrinsic band gap emission because of the sp^2 conjugation in the cores and extrinsic fluorescence from the surface states,[41−45] the hybridization of the OLC carbon backbone and adherent surface functional groups may introduce surface states that serve as emissive traps, thus resulting in the wavelength variable emissions as shown in Figure 5.

PL quenching appears after loading the $Cd_{0.5}Zn_{0.5}S$ QDs onto the OLC (Figure 5c). Compared with the strong emissions at 476 and 530 nm, respectively, for pure OLC and $Cd_{0.5}Zn_{0.5}S$ QDs, the composites only show a weak emission at 530 nm when excited at 380 nm, corresponding to the band−band emission of $Cd_{0.5}Zn_{0.5}S$. The significant depression of the $Cd_{0.5}Zn_{0.5}S$ emission and the quenching of the OLC emission suggest that charge separation occurs at the $Cd_{0.5}Zn_{0.5}S$/OLC interfaces. This can be further confirmed by the extended radiation lifetime of the $Cd_{0.5}Zn_{0.5}S$/OLC composites compared with those of pure $Cd_{0.5}Zn_{0.5}S$ QDs and pure OLCs (Figure 5d). Compared with 1.83 ns of pure $Cd_{0.5}Zn_{0.5}S$, the composite has a longer lifetime of 1.88 ns.

3.4. Band Diagram and Mechanism Discussions. To examine this, the band diagram of the $Cd_{0.5}Zn_{0.5}S$/OLC nanocomposite was studied by VB XPS and Mott−Schottky curve (Figures S6 and S7). For pure individual $Cd_{0.5}Zn_{0.5}S$ and

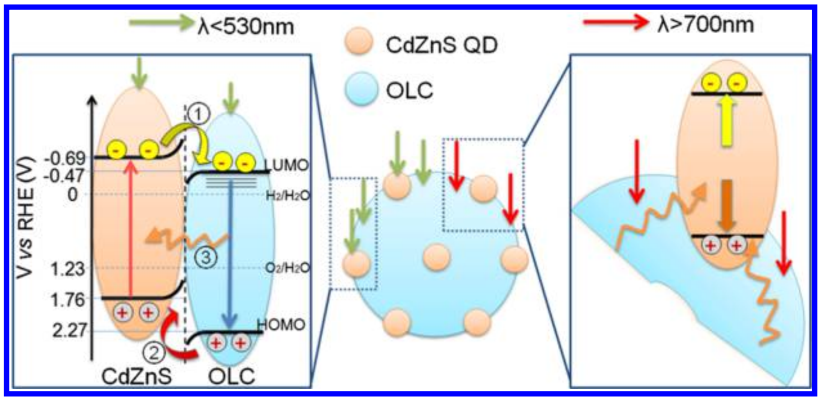

Figure 6. Schematic band diagram, charge, and energy transfer of $Cd_{0.5}Zn_{0.5}S$/OLC nanocomposite under light irradiation with different wavelength.

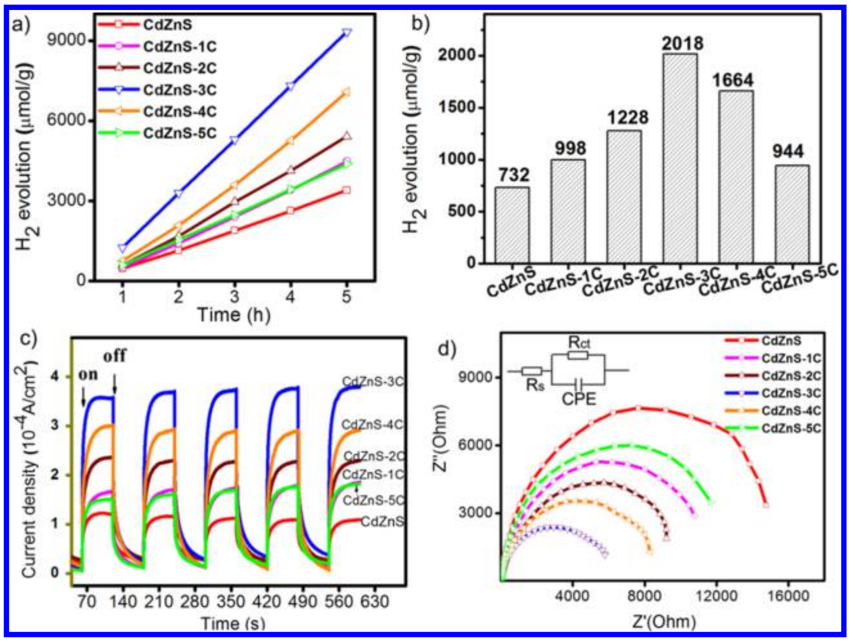

Figure 7. OLC content-dependent photocatalytic property. (a,b) H_2 evolution of $Cd_{0.5}Zn_{0.5}S/x$C (x = 1−5) nanocomposites under the irradiation of visible light (300 mW/cm^2). (c) Photocurrent response of the samples with different content of the OLC under the irradiation of visible light in a three-electrode system. (d) EIS spectra of the samples with different content of the OLC, and the inset shows the equivalent circuit.

the OLC before they are in contact with each other in the composite, the flat band potential (the difference between Fermi level and water reduction potential) can be estimated as −0.40 and −0.05 V versus RHE. The VB maximum of $Cd_{0.5}Zn_{0.5}S$ and the highest occupied molecular orbital (HOMO) level of the OLC are estimated to be 1.41 and 2.27 V (vs RHE), respectively. On the basis of the band gap of 2.45 eV obtained from the Tauc plot in Figure S5, the conduction band minimum (CBM) of $Cd_{0.5}Zn_{0.5}S$ can be estimated as −1.04 V versus RHE. Taking the PL emission at 452 nm (λ_{ex} = 340 nm) as the nearest band−band transition of 2.74 eV for the OLC, the lowest unoccupied molecular orbital (LUMO) level of the OLC can be estimated as −0.47 V versus RHE, which is consistent with the reported results.[14,46] After the QD/OLC composite is formed, the Fermi levels of $Cd_{0.5}Zn_{0.5}S$ and the OLC are flattened and form a type-II band alignment at the $Cd_{0.5}Zn_{0.5}S$/C interface (Figures S7b and 6), and an obvious down shift in the energy levels of $Cd_{0.5}Zn_{0.5}S$ occurs once $Cd_{0.5}Zn_{0.5}S$ contacts with the OLC. Between the HOMO and LUMO levels of the OLC, many trap levels are known to exist as induced by the surface functional groups.[41−45]

Given the type-II band alignment between $Cd_{0.5}Zn_{0.5}S$ and the OLC, the enhanced photocatalytic response of the $Cd_{0.5}Zn_{0.5}S$/OLC composite compared with pure $Cd_{0.5}Zn_{0.5}S$ can be attributed to the two processes (Figure 6) occurred under the respective illumination of visible and NIR light. The first process is illustrated in the left panel of Figure 6. When the composite is excited by light photon of λ_{ex} < 530 nm, the photogenerated electron is driven from the CBM of QDs to the LUMO or trap levels of the OLC in the composite (step 1), whereas the photogenerated hole from the OLC nanoparticles can be reversely transferred to nearby QDs (step 2). Meanwhile, the recombination of the photogenerated carriers in the OLC may also occur, after which the emission energy can be further absorbed by the adjacent QDs (step 3). Because steps 1 and 2 can help prolong the radiation lifetime and depress the emission intensity, and the energy transfer step 3 may consume the fluorescence intensity and benefit to utilize the light preferably for charge-carrier generation in the QDs; these steps finally result in the depression of the fluorescence and extended lifetime of charge carrier in the QDs. However, nonradiative recombination induced by defect states at the $Cd_{0.5}Zn_{0.5}S$/OLC interfaces cannot be completely excluded. On the other hand, there is another energy transfer process that accounts for the photocatalytic H_2 evolution in the NIR region. As shown by the right panel in Figure 6, when excited by the light of $\lambda > 700$ nm, the OLC will emit a short wavelength light of $\lambda_{em} < 530$ nm because of the UCPL property, which can be readily absorbed by the neighboring $Cd_{0.5}Zn_{0.5}S$ QDs, then generating electrons and holes for the HER behavior upon the NIR region light.

3.5. Performance Dependence on the Ratio between the OLC and $Cd_{0.5}Zn_{0.5}S$. The effect of the OLC-to-$Cd_{0.5}Zn_{0.5}S$ ratio on the photocatalytic H_2 generation property was studied systematically. As shown in Figure 7a,b, the hydrogen evolution rate first increases, then decreases with the OLC content x increasing from 1 to 5, and achieves an optimum rate of 2018 μmol/h/g at x of 3. The trend remains the same as the transient current evolution presented in Figure 7c. At the same time, the EIS result (Figure 7d) suggests that the charge-transfer resistance (R_{ct}) first decreases, then increases with the OLC, and reaches the lowest value at $x = 3$. Higher x value means more OLCs were introduced into the composites (Figure S8). Given that once the surface of the $Cd_{0.5}Zn_{0.5}S$ QDs starts to be wrapped by the OLCs, both the photon energy transfer from the OLCs to the QDs and charge separation at the OLC/QD interface can be satisfied. This will increase the light utilization and decrease the carrier recombination and thus promote the photocatalytic H_2 evolution and transient current accordingly. However, the defective nature of the OLCs, particularly those at the QD/OLC interfaces, may become nonradiative recombination centers for the photogenerated carriers in the QDs. The experimental results suggest that an optimized interface is formed between the QD and the OLC at $x = 3$.

4. CONCLUSIONS

The OLC nanoparticles of ~30 nm with both UCPL and DCPL characters were adopted as matrixes for loading 6.9 nm-sized $Cd_{0.5}Zn_{0.5}S$ QDs for noble metal-free photocatalytic H_2 generation. Besides the enhanced absorption over the visible and NIR range light (compared with pure $Cd_{0.5}Zn_{0.5}S$), the charge separation, transfer, and energy transfer mechanisms are disclosed for the $Cd_{0.5}Zn_{0.5}S$/OLC composites based on the type-II band alignment between the $Cd_{0.5}Zn_{0.5}S$ and OLC. By tuning the ratio between the OLCs and $Cd_{0.5}Zn_{0.5}S$ QDs, an optimum photon energy transfer from the OLCs to QDs and charge separation at the OLC/QD interface can be achieved, leading to a maximum H_2 generation rate of 2018 μmol/h/g upon visible light and appreciable H_2 evolution rate of 58.6 μmol/h/g upon the NIR light. The $Cd_{0.5}Zn_{0.5}S$ QDs-on-OLC structure allows the manipulation of the QD/OLC interface for efficient light utilization and photon-generated charge-carrier separation, serving as a promising strategy for developing noble metal-free photocatalysts with a high-efficiency H_2 evolution.

ASSOCIATED CONTENT

Supporting Information

The Supporting Information is available free of charge on the ACS Publications website at DOI: 10.1021/acsami.7b05592.

> The photocatalytic evaluation system; XRD patterns; FTIR spectra; Tauc plot; Mott−Schottky curves; VB XPS spectra; band diagram; XPS survey scans; and TEM pictures and particle size distribution (PDF)

AUTHOR INFORMATION

Corresponding Authors

*E-mail: xnwang2006@hotmail.com (X.W.).
*E-mail: liquan@phy.cuhk.edu.hk (Q.L.).

ORCID

Xina Wang: 0000-0003-3350-6043
Hao Wang: 0000-0002-4894-7653

Notes

The authors declare no competing financial interest.

ACKNOWLEDGMENTS

This work was supported by the National Natural Science Foundation of China (no. 51472080, 11104097) and Open Research Fund Program of the State Key Laboratory of Low-Dimensional Quantum Physics (no. KF201411).

REFERENCES

(1) Hisatomi, T.; Kubota, J.; Domen, K. Recent Advances in Semiconductors for Photocatalytic and Photoelectrochemical Water Splitting. *Chem. Soc. Rev.* **2014**, *43*, 7520−7535.

(2) Moriya, Y.; Takata, T.; Domen, K. Recent Progress in the Development of (Oxy)Nitride Photocatalysts for Water Splitting under Visible-Light Irradiation. *Coord. Chem. Rev.* **2013**, *257*, 1957−1969.

(3) Yao, L.; Wei, D.; Ni, Y.; Yan, D.; Hu, C. Surface Localization of CdZnS Quantum Dots onto 2D g-C_3N_4 Ultrathin Microribbons: Highly Efficient Visible Light-Induced H_2-Generation. *Nano Energy* **2016**, *26*, 248−256.

(4) Wu, J.-C.; Zheng, J.; Zacherl, C. L.; Wu, P.; Liu, Z.-K.; Xu, R. Hybrid Functionals Study of Band Bowing, Band Edges and Electronic Structures of $Cd_{1-x}Zn_xS$ Solid Solution. *J. Phys. Chem. C* **2011**, *115*, 19741−19748.

(5) Wang, L.; Wang, W.; Shang, M.; Yin, W.; Sun, S.; Zhang, L. Enhanced Photocatalytic Hydrogen Evolution under Visible Light Over $Cd_{1-x}Zn_xS$ Solid Solution with Cubic Zinc Blend Phase. *Int. J. Hydrogen Energy* **2010**, *35*, 19−25.

(6) Wang, H.; Li, Y.; Shu, D.; Chen, X.; Liu, X.; Wang, X.; Zhang, J.; Wang, H. CoPtx-Loaded $Zn_{0.5}Cd_{0.5}S$ Nanocomposites for Enhanced Visible Light Photocatalytic H_2 Production. *Int. J. Energy Res.* **2016**, *40*, 1280−1286.

(7) Gaikwad, A. P.; Tyagi, D.; Betty, C. A.; Sasikala, R. Photocatalytic and Photo Electrochemical Properties of Cadmium Zinc Sulfide Solid Solution in the Presence of Pt and RuS_2 Dual Co-catalysts. *Appl. Catal., A* **2016**, *517*, 91−99.

(8) Aydemir, M.; Akyüz, D.; Agopcan, B.; Şener, M. K.; Albayrak, F. K.; Sarıoğlu, C.; Koca, A. Photocatalytic−Electrocatalytic Dual Hydrogen Production System. *Int. J. Hydrogen Energy* **2016**, *41*, 8209−8220.

(9) Ma, X.; Jiang, Q.; Guo, W.; Zheng, M.; Xu, W.; Ma, F.; Hou, B. Fabrication of g-C_3N_4/Au/CdZnS Z-scheme Photocatalyst to Enhance Photocatalysis Performance. *RSC Adv.* **2016**, *6*, 28263−28269.

(10) Zhang, J.; Yu, J.; Jaroniec, M.; Ru Gong, J. Noble Metal-Free Reduced Graphene Oxide-$Zn_xCd_{1-x}S$ Nanocomposite with Enhanced Solar Photocatalytic H_2-Production Performance. *Nano Lett.* **2012**, *12*, 4584−4589.

(11) Gong, B.; Lu, Y.; Wu, P.; Huang, Z.; Zhu, Y.; Dang, Z.; Zhu, N.; Lu, G.; Huang, J. Enhanced Photocatalytic Activity Over $Cd_{0.5}Zn_{0.5}S$ with Stacking Fault Structure Combined with Cu^{2+} Modified Carbon Nanotubes. *Appl. Surf. Sci.* **2016**, *365*, 280−290.

(12) Chen, Y.; Guo, L. Highly Efficient Visible-Light-Driven Photocatalytic Hydrogen Production From Water Using $Cd_{0.5}Zn_{0.5}S$/TNTs (Titanate Nanotubes) Nanocomposites without Noble Metals. *J. Mater. Chem.* **2012**, *22*, 7507−7514.

(13) Liu, J.; Liu, Y.; Liu, N.; Han, Y.; Zhang, X.; Huang, H.; Lifshitz, Y.; Lee, S.-T.; Zhong, J.; Kang, Z. Metal-Free Efficient Photocatalyst for Stable Visible Water Splitting Via a Two-Electron Pathway. *Science* **2015**, *347*, 970−974.

(14) Xu, X.; Bao, Z.; Zhou, G.; Zeng, H.; Hu, J. Enriching Photoelectrons Via Three Transition Channels in Amino-Conjugated Carbon Quantum Dots to Boost Photocatalytic Hydrogen Generation. *ACS Appl. Mater. Interfaces* **2016**, *8*, 14118−14124.

(15) Tian, J.; Leng, Y.; Zhao, Z.; Xia, Y.; Sang, Y.; Hao, P.; Zhan, J.; Li, M.; Liu, H. Carbon Quantum Dots/Hydrogenated TiO_2 Nanobelt Heterostructures and Their Broad Spectrum Photocatalytic Properties under UV, Visible, and Near-Infrared Irradiation. *Nano Energy* **2015**, *11*, 419−427.

(16) Yeh, T.-F.; Teng, C.-Y.; Chen, S.-J.; Teng, H. Nitrogen-Doped Graphene Oxide Quantum Dots as Photocatalysts for Overall Water-Splitting Under Visible Light Illumination. *Adv. Mater.* **2014**, *26*, 3297−3303.

(17) Ugarte, D. Curling and Closure of Graphitic Networks under Electron-Beam Irradiation. *Nature* **1992**, *359*, 707−709.

(18) Wang, R.; Lu, K.-Q.; Tang, Z.-R.; Xu, Y.-J. Recent Progress in Carbon Quantum Dots: Synthesis, Properties and Applications in Photocatalysis. *J. Mater. Chem. A* **2017**, *5*, 3717−3734.

(19) Li, X.; Liu, Y.; Song, X.; Wang, H.; Gu, H.; Zeng, H. Intercrossed Carbon Nanorings with Pure Surface States as Low-Cost and Environment-Friendly Phosphors for White-Light-Emitting Diodes. *Angew. Chem., Int. Ed.* **2015**, *54*, 1759−1764.

(20) Li, H.; He, X.; Kang, Z.; Huang, H.; Liu, Y.; Liu, J.; Lian, S.; Tsang, C. H. A.; Yang, X.; Lee, S.-T. Water-Soluble Fluorescent Carbon Quantum Dots and Photocatalyst Design. *Angew. Chem., Int. Ed.* **2010**, *49*, 4430−4434.

(21) Zhu, S.; Meng, Q.; Wang, L.; Zhang, J.; Song, Y.; Jin, H.; Zhang, K.; Sun, H.; Wang, H.; Yang, B. Highly Photoluminescent Carbon Dots for Multicolor Patterning, Sensors, and Bioimaging. *Angew. Chem.* **2013**, *125*, 4045−4049.

(22) Li, Y.; Hu, Y.; Zhao, Y.; Shi, G.; Deng, L. E.; Hou, Y.; Qu, L. T. An Electrochemical Avenue to Green-Luminescent Graphene Quantum Dots as Potential Electron-Acceptors for Photovoltaics. *Adv. Mater.* **2011**, *23*, 776−780.

(23) Tripathi, K. M.; Bhati, A.; Singh, A.; Gupta, N. R.; Verma, S.; Sarkar, S.; Sonkar, S. K. From the Traditional Way of Pyrolysis to Tunable Photoluminescent Water Soluble Carbon Nano-Onions for Cell Imaging and Selective Sensing of Glucose. *RSC Adv.* **2016**, *6*, 37319−37329.

(24) Yu, H.; Zhao, Y.; Zhou, C.; Shang, L.; Peng, Y.; Cao, Y.; Wu, L.-Z.; Tung, C.-H.; Zhang, T. Carbon Quantum Dots/TiO_2 Composites for Efficient Photocatalytic Hydrogen Evolution. *J. Mater. Chem. A* **2014**, *2*, 3344−3351.

(25) Wang, J.; Ng, Y. H.; Lim, Y.-F.; Ho, G. W. Vegetable-Extracted Carbon Dots and Their Nanocomposites for Enhanced Photocatalytic H_2 Production. *RSC Adv.* **2014**, *4*, 44117−44123.

(26) Li, Q.; Cui, C.; Meng, H.; Yu, J. Visible-Light Photocatalytic Hydrogen Production Activity of $ZnIn_2S_4$ Microspheres Using Carbon Quantum Dots and Platinum as Dual Co-catalysts. *Chem.—Asian J.* **2014**, *9*, 1766−1770.

(27) Yang, P.; Zhao, J.; Wang, J.; Cao, B.; Li, L.; Zhu, Z. Construction of Z-scheme Carbon Nanodots/WO_3 with Highly Enhanced Photocatalytic Hydrogen Production. *J. Mater. Chem. A* **2015**, *3*, 8256−8259.

(28) Liu, J.; Zhang, H.; Tang, D.; Zhang, X.; Yan, L.; Han, Y.; Huang, H.; Liu, Y.; Kang, Z. Carbon Quantum Dot/Silver Nanoparticle/Polyoxometalate Composites as Photocatalysts for Overall Water Splitting in Visible Light. *ChemCatChem* **2014**, *6*, 2634−2641.

(29) Xia, X.; Deng, N.; Cui, G.; Xie, J.; Shi, X.; Zhao, Y.; Wang, Q.; Wang, W.; Tang, B. NIR Light Induced H_2 Evolution by a Metal-Free Photocatalyst. *Chem. Commun.* **2015**, *51*, 10899−10902.

(30) Li, H.; Liu, R.; Liu, Y.; Huang, H.; Yu, H.; Ming, H.; Lian, S.; Lee, S.-T.; Kang, Z. Carbon Quantum Dots/Cu_2O Composites with Protruding Nanostructures and Their Highly Efficient (Near) Infrared Photocatalytic Behavior. *J. Mater. Chem.* **2012**, *22*, 17470−17475.

(31) Lin, Z.; Li, J.; Zheng, Z.; Yu, L.; Wang, C.; Yang, G. A Floating Sheet for Efficient Photocatalytic Water Splitting. *Adv. Energy Mater.* **2016**, *6*, 1600510.

(32) Lin, Z.; Xiao, J.; Li, L.; Liu, P.; Wang, C.; Yang, G. Nanodiamond-Embedded p-Type Copper(I) Oxide Nanocrystals for Broad-Spectrum Photocatalytic Hydrogen Evolution. *Adv. Energy Mater.* **2016**, *6*, 1501865.

(33) Dubey, P.; Tripathi, K. M.; Sonkar, S. M. Gram Scale Synthesis of Green Fluorescent Water-Soluble Onion-Like Carbon Nanoparticles from Camphor and Polystyrene Foam. *RSC Adv.* **2014**, *4*, 5838−5844.

(34) Kudo, A.; Miseki, Y. Heterogeneous Photocatalyst Materials for Water Splitting. *Chem. Soc. Rev.* **2009**, *38*, 253−278.

(35) Sethi, R.; Sharma, P. K.; Pandey, A. C.; Kumar, L. Raman Studies on Ag-ion Doped CdZnS Luminescent Alloy Quantum Dots. *Chem. Phys. Lett.* **2010**, *495*, 63−68.

(36) Permatasari, F. A.; Aimon, A. H.; Iskandar, F.; Ogi, T.; Okuyama, K. Role of C−N Configurations in the Photoluminescence of Graphene Quantum Dots Synthesized by a Hydrothermal Route. *Sci. Rep.* **2016**, *6*, 21042.

(37) Kozlova, E. A.; Cherepanova, S. V.; Markovskaya, D. V.; Saraev, A. A.; Gerasimov, E. Y.; Parmon, V. N. Novel Photocatalysts Pt/$Cd_{1-x}Zn_xS$/ZnO/$Zn(OH)_2$: Activation During Hydrogen Evolution from Aqueous Solutions of Ethanol under Visible light. *Appl. Catal., B* **2016**, *183*, 197−205.

(38) Zhang, J.; Wang, P.; Sun, J.; Jin, Y. High-Efficiency Plasmon-enhanced and Graphene-Supported Semiconductor/metal Core−Satellite Hetero-Nanocrystal Photocatalysts for Visible-Light Dye Photodegradation and H2 Production from Water. *ACS Appl. Mater. Interfaces* **2014**, *6*, 19905−19913.

(39) Li, W.; Lee, J. R.; Jäckel, F. Simultaneous Optimization of Colloidal Stability and Interfacial Charge Transfer Efficiency in Photocatalytic Pt/CdS Nanocrystals. *ACS Appl. Mater. Interfaces* **2016**, *8*, 29434−29441.

(40) Yin, X.-L.; Li, L.-L.; Jiang, W.-J.; Zhang, Y.; Zhang, X.; Wan, L.-J.; Hu, J.-S. MoS_2/CdS Nanosheets-on-Nanorod Heterostructure for Highly Efficient Photocatalytic H_2 Generation under Visible Light Irradiation. *ACS Appl. Mater. Interfaces* **2016**, *8*, 15258−15266.

(41) Li, X.; Liu, Y.; Song, X.; Wang, H.; Gu, H.; Zeng, H. Intercrossed Carbon Nanorings with Pure Surface States as Low-Cost and Environment-Friendly Phosphors for White-Light-Emitting Diodes. *Angew. Chem., Int. Ed.* **2014**, *54*, 1759−1764.

(42) Zhu, S.; Song, Y.; Zhao, X.; Shao, J.; Zhang, J.; Yang, B. The Photoluminescence Mechanism in Carbon Dots (Graphene Quantum Dots, Carbon Nanodots, and Polymer Dots): Current State and Future Perspective. *Nano Res.* **2015**, *8*, 355−381.

(43) Xu, X.; Ray, R.; Gu, Y.; Ploehn, H. J.; Gearheart, L.; Raker, K.; Scrivens, W. A. Electrophoretic Analysis and Purification of Fluorescent Single-Walled Carbon Nanotube Fragments. *J. Am. Chem. Soc.* **2004**, *126*, 12736−12737.

(44) Li, H.; Kang, Z.; Liu, Y.; Lee, S.-T. Carbon Nanodots: Synthesis, Properties and Applications. *J. Mater. Chem.* **2012**, *22*, 24230−24253.

(45) Yu, H.; Shi, R.; Zhao, Y.; Waterhouse, G. I. N.; Wu, L.-Z.; Tung, C.-H.; Zhang, T. Smart Utilization of Carbon Dots in Semiconductor Photocatalysis. *Adv. Mater.* **2016**, *28*, 9454−9477.

(46) Ming, H.; Ma, Z.; Liu, Y.; Pan, K.; Yu, H.; Wang, F.; Kang, Z. Large Scale Electrochemical Synthesis of High Quality Carbon Nanodots and Their Photocatalytic Property. *Dalton Trans.* **2012**, *41*, 9526−9531.